

# Assessing the Collective Dynamics of Motile Cilia in Cultures of Human Airway Cells by Multiscale DDM

Luigi Feriani,<sup>1</sup> Maya Juenet,<sup>1</sup> Cedar J. Fowler,<sup>2,3</sup> Nicolas Bruot,<sup>1</sup> Maurizio Chioccioli,<sup>1</sup> Steven M. Holland,<sup>3</sup> Clare E. Bryant,<sup>2</sup> and Pietro Cicuta<sup>1,\*</sup>

<sup>1</sup>Cavendish Laboratory, University of Cambridge, Cambridge, United Kingdom; <sup>2</sup>Laboratory of Clinical Infectious Diseases, National Institute of Health, Bethesda, Maryland; and <sup>3</sup>Department of Veterinary Medicine, University of Cambridge, Cambridge, United Kingdom

**ABSTRACT** The technique of differential dynamic microscopy is extended here, showing that it can provide a powerful and objective method of video analysis for optical microscopy videos of *in vitro* samples of live human bronchial epithelial ciliated cells. These cells are multiciliated, with motile cilia that play key physiological roles. It is shown that the ciliary beat frequency can be recovered to match conventional analysis, but in a fully automated fashion. Furthermore, it is shown that the properties of spatial and temporal coherence of cilia beat can be recovered and distinguished, and that if a collective traveling wave (the metachronal wave) is present, this has a distinct signature and its wavelength and direction can be measured.

## INTRODUCTION

Cilia are cell organelles, slender protuberances that stick out of the surface of many eukaryotic cells (1,2). They are covered in cellular membrane, and contain a bundle of microtubules called the “axoneme”. The axoneme can have two structures: 9 + 2, with nine doublet microtubules arranged radially around two central singlet microtubules; and 9 + 0, where the two central microtubules are missing. Their structure underpins their function. Cilia missing the two central microtubules are called “primary cilia”; they are not motile and have been reported to act as chemical or mechanical sensors (3–5).

The motile cilia are structurally conserved, allowing motility in single cell eukaryotes and transport of fluids along cell epithelia in multicellular organisms (6). Understanding cilia motility requires concepts and a deep understanding from many fields, from cell biology and medicine, to fluid dynamics, soft matter, and nonlinear physics (7). Questions range over many scales: at the level of the individual organelle, we want to know the metabolic path in ciliary motion, the molecular structures involved in this organelle’s

assembly and function, and how a cilia waveform for efficient beating is achieved (8,9); at the level of tissues, how many of these beating filaments coordinate with each other, the importance of arrangement, density, fluid physical parameters, and then the role played by cilia-generated flows in key biological processes such as symmetry breaking and onset of planar cell polarity in development (10–14). The medical community has parallel questions in understanding how cilia malfunction is related to various pathologies (15–18), and very practically how to relate imaging of ciliary beating to the diagnosis of such pathologies. Finally, cilia are studied in engineering to replicate biomimetically their capacity of creating flow in low Reynolds number environments (19), or even to try and build microrobots (20).

A crucial element from the scenario described above is how the coordinated motion of cilia arises, and how the collective state (e.g., traveling wave) properties relate to the mechanisms and mechanics of the individual beating filaments. This can be addressed either with a bottom-up approach, modeling each cilium with something simpler and studying synchronization of a few model cilia (our group’s previous work in that direction is reviewed in (7)), or with a top-down approach, i.e., characterizing the collective motion in real systems and trying to infer some information about the properties at the single cilium level. In either case, one needs to appreciate that the single cilium itself is a complex nonlinear dynamical system functioning out of thermal equilibrium, and described by many degrees of freedom (21). Cilia within the same cell are mechanically

Submitted December 23, 2016, and accepted for publication May 22, 2017.

\*Correspondence: [pc245@cam.ac.uk](mailto:pc245@cam.ac.uk)

Maya Juenet’s present address is Laboratory for Vascular Translational Science, Paris Cedex 18, France.

Nicolas Bruot’s present address is Institute of Industrial Science, The University of Tokyo, Komaba, Meguro-ku, Tokyo, Japan.

Editor: Jeffrey Fredberg.

<http://dx.doi.org/10.1016/j.bpj.2017.05.028>

© 2017 Biophysical Society.

connected through the cytoskeleton (6), and are immersed in a fluid that, in the case of the airways, displays viscoelasticity and complex heterogeneous composition critical for mucociliary clearance (22). The conclusion that can be drawn from model experiments in our group so far (7) is that hydrodynamic coupling is sufficient to promote strong synchronization through various mechanisms, and in simple systems it is possible to link the emergent behavior to the details of how each cilium is driven (23,24), and how cilia are spatially arranged relative to each other (25,26). In general, we do not fully know how the collective dynamics yield such a fascinating emergent behavior at a tissue scale.

When cilia are arranged in a tight 2D array as in human airways, or on the outer surface of *Paramecium*, a particular type of collective motion has been observed: neighboring cilia beat with a constant small phase difference. This yields without a central organizing node (i.e., just out of local rules) a propagating pattern called a “metachronal wave” (27–30). Cilia beat is optimized for fluid transport (9), and according to recent theoretical studies (31), metachronal waves are retrieved when trying to optimize the net flow generated by a cilia array, suggesting that hydrodynamic coupling plays a fundamental role in the swimming of microorganisms and in mucociliary clearance in human airways. Other studies also strongly suggest hydrodynamic coupling to be the mechanism through which cilia metachronality arises (32,33).

Understanding the physics of how the coordinated behavior of cilia emerges is still an open question, currently studied both on model organisms (34), and on model systems (7,35,36).

The lungs and airways are kept pathogen- and dust free thanks to the process of mucociliary clearance (37). The walls of the airways are covered by an epithelium composed by two types of cells: ciliated cells (~60–80%) and mucus-producing goblet cells. Cilia are immersed in the periciliary layer (PCL), ~6  $\mu\text{m}$  thick. According to a study in 2012 (22), the periciliary layer is occupied by a brushlike structure of macromolecules, namely membrane-spanning mucins and tethered mucopolysaccharides, with a mesh size that depends on the distance from the surface of the ciliated cells; the PCL is then topped by a layer of mucus, with a lower osmotic modulus ensuring a stable hydration level of the PCL (and therefore its constant height) over a range of dehydration states of the airway surface. From a rheological point of view, the mucus is a gel whose viscoelastic properties are strongly dependent on its state of hydration (37).

Mucus is transported out of the airways by mucociliary clearance mechanisms, which rely on the interaction between cilia, the rheologically complex PCL, and the gel-like layer of mucus. It was observed (38) that ideal condition for mucociliary clearance is a temperature of 37°C with 100% humidity. The velocity of mucus in human airways is not known exactly; measurements using different techniques reported

3.6–25 mm/min for mucus in the trachea, whereas the only measured value in bronchi is 2.4 mm/min (39).

The ciliated tissue of the airways is studied also from a medical point of view: conditions such as cystic fibrosis and primary cilia dyskinesia can disrupt the airway clearance mechanism, causing severe consequences such as lung infections and respiratory insufficiency. Also, the very common asthma is linked to altered airway clearance (40).

This article presents, to our knowledge, a new method for the characterization of collective cilia dynamics, focusing on epithelial cell arrays that are typically grown at the air-liquid interface (ALI) condition. In [Video Analysis of Cilia Dynamics](#), an overview is given of existing image analysis approaches. [Cell Culture and Imaging](#) describes the cell culture and imaging protocols. The core method is presented in [Development of a New Video Analysis Procedure: Differential Dynamic Microscopy](#), where the differential dynamic microscopy (DDM)-based approach is tested on cell cultures. [Results and Discussion](#) goes over the quantities measurable by DDM. In [Appendix A: Testing DDM on Synthetic Datasets](#), the potential of the method, beyond what we can show given current experimental data, is tested against computer generated datasets.

## MATERIALS AND METHODS

### Video analysis of cilia dynamics

Airway cells from human patients can be obtained by biopsy or nose scrape, and then either observed directly or cultured to grow as an in vitro epithelium, typically as the air-liquid interface. The latter is the most relevant model system for investigating collective dynamics (coordination across many cells) and mucociliary clearance.

The tools that physicians can use to analyze microscopy videos of ciliated cells are limited. A standard is the commercial software Sisson-Ammons Video Analysis (SAVA; Ammons Engineering, <http://www.ammonsengineering.com/SAVA/sava.html>) (41), which measures the cilia beat frequencies (CBF) in a user-selected area. The selected area is small (typically  $4 \times 4$  px), and CBF is measured by Fourier transforming the signal of the pixel intensity over the video. The software thus requires input from the user, i.e., a human resource and possible introduction of bias (e.g., the human eye is naturally drawn toward fast-moving objects). More importantly, and unlike the method presented in this work, this type of analysis does not probe the spatial correlation in the phase of beating cilia, thus ignores information about metachronal coordination.

Historically, a few approaches have been explored for quantitative measurements on ciliated cells. Initially, CBF would be measured using a photomultiplier or a photodiode, analyzing the changes in the intensity of the light passing through beating cilia (42–44). With high-frame-rate cameras it became possible to record high-speed videos of beating cilia, for subsequent analysis. The most straightforward method to measure CBF became therefore to measure the period over a few beating cycles (45). This was done by visual inspection of the slowed-down video. The ability to record and store high-speed microscopy video of beating cilia encouraged development of new algorithms for CBF measurement: most extract the CBF via fast Fourier transform (FFT) analysis of pixel intensity over time, either in user-selected regions of interest (41,46,47) or in the entire field of view (48). This method, however, only performs a temporal analysis. An alternative approach is to use an optical flow algorithm: After mapping the movements of objects in-between subsequent frames

on a vector field, one can obtain the CBF from the displacement signal via FFT (49,50) or peak detection (51). Other tools, also based on optical flow, try and extract more than just the CBF from microscopy videos in which cilia are seen from the side: in Mantovani et al. (52), the beating direction is retrieved, whereas Quinn et al. (53) even attempts an automatic diagnosis of primary cilia dyskinesia based on the decomposition of ciliary motion as measured in a location chosen by the user into quantitative elemental components. Phase-correlation measurement between physically separated points in the sample are instead at the base of methods aimed to measure the parameters of metachronal waves (27,54–58). A very thorough work by Ryser et al. (59) showed that reflected light microscopy videos of excised mammalian and avian ciliated tissues can be analyzed to measure both the CBF and the direction and wavelength of metachronal wave. The analysis presented in Ryser et al. (59) and employed successively in Schätz et al. (60) is very well suited to study samples in which the metachronal coordination is well developed: first, the sample's CBF is measured via FFT, then the metachronal coordination is characterized using space-time correlation functions and the time evolution of the phase of the recorded signal. A different approach is, however, needed when working with ALI cultures, which is the standard condition for culturing in-vitro human airway epithelial cells. Here cilia are usually not aligned and often only show isolated patches of good metachronal coordination on the scale of a few cells. This is where the method we suggest can be very powerful, in that it performs simultaneously and in a completely automated fashion both a temporal and spatial analysis on top-view high-speed microscopy videos of a layer of ciliated cells. Without requiring any input from the user, DDM can not only 1) reliably measure the CBF of a sample, but also 2) quantify to what extent the cilia are synchronized across the field of view, 3) identify metachronal waves (if present), and 4) measure their wavelength and direction of propagation.

## Cell culture and imaging

*Culture of ciliated cells at the air-liquid interface.* Commercially available Normal Human Bronchial Epithelial cells provided by Lonza (Cat. No. CC-2540; Walkersville, MD) were grown at the ALI following a protocol issued by the selling company. After defrosting,  $9.5 \times 10^4$  cells were seeded into 6.5-mm collagen-coated polyester Transwell inserts (12-well inserts with a pore size of  $0.4 \mu\text{m}$ ; Corning, Lowell, MA) with basal ALI media (Cat. No. B-ALI-BulletKit; Lonza). When confluent, the transwells were shifted to ALI culture by removing the apical media and maintaining  $800 \mu\text{L}$  ALI media in the basal compartment. The media were exchanged every other day. Mucociliary differentiation and cilia beating occurred within 4 weeks.

*Imaging.* Normal Human Bronchial Epithelial cells were imaged in bright field using a  $63\times$  glycerol objective with a  $1.5\times$  internal magnification on a DM IRBE inverted microscope (Leica Microsystems, Bannockburn, IL) on a vibration-dampened table. An area scan high-speed monochromatic digital video camera (model No. A602f-2; Basler, Ahrensburg, Germany) was used for image and video acquisition, recording a  $\sim 2.56$  s video with a resolution of  $720 \times 480$  pixel (px) and 100 fps frame rate. At this  $94.5\times$  magnification,  $1 \text{ px} = 0.161 \mu\text{m}$ . The inverse pixel size  $k = 6.2 \mu\text{m}^{-1}$  and the frame size  $L = 480$  px (the algorithm was coded to work on square images, therefore  $L$  is the size of the shortest side of the image) define the spatial sampling frequency  $q_{\min} = 2\pi k/L = 0.081 \mu\text{m}^{-1}$ .

All imaging was done at  $37^\circ\text{C}$  in ALI media. At each time point of the experiment,  $\sim 40$  fields of view of each sample were imaged. All samples were kept at  $37^\circ\text{C}$  and 5%  $\text{CO}_2$  and in ALI media throughout the experiment and imaging.

*Commercially available assay and imaging thereof.* The videos analyzed for DDM-based Detection of Metachronal Waves and Length Scale of Synchronization: Real Data were obtained from different samples than those described in Culture of Ciliated Cells at the Air-Liquid Interface, and imaged differently than described in Imaging. A healthy human airway epithelium reconstituted in-vitro (MucilAir) was purchased from

Epithelix Sàrl (Geneva, Switzerland) and maintained following the protocol provided by the company. The layer of ciliated cells (much more densely ciliated than was possible via the method of Culture of Ciliated Cells at the Air-Liquid Interface) was then imaged in bright field on a Ti-E inverted microscope (Nikon, Tokyo, Japan) equipped with a  $40\times$  dry objective (NA = 0.95; Nikon). High speed videos were then recorded using a CMOS camera (model No. GS3-U3-23S6M-C; Point Grey Research/FLIR Integrated Imaging Solutions (Machine Vision), Richmond, British Columbia, Canada) connected to a LINUX workstation running a custom video grabbing software developed in house. The videos have a resolution of  $1024 \times 1024$  pixel and 150 fps frame rate. This magnification yields a  $0.146 \mu\text{m}/\text{px}$  ratio and, together with the frame size  $L = 1024$  px, a spatial sampling frequency  $q_{\min} = 0.042 \mu\text{m}^{-1}$ .

## Development of a new video analysis procedure: differential dynamic microscopy

This section describes, to our knowledge, a new approach for user-independent characterization of cilia collective dynamics. The code has been implemented in MATLAB (The MathWorks, Natick, MA), and the DDM algorithm is applied to analyze videos from the dataset described in Imaging. The first goal of the analysis is to obtain an unbiased measurement of the ciliary beat frequency, which can be compared to previous analysis approaches.

A discussion on how to perform a more thorough analysis on the sample to retrieve additional parameters will be carried on in the Results and Discussion and Appendix A: Testing DDM on Synthetic Datasets. Figures that illustrate the analysis all refer to the same video.

The technique of DDM was invented fairly recently to characterize dynamics in colloidal suspensions (61,62) and relies on Fourier analysis of difference images. Here we build on this approach, developing what might be called a “multiscale-DDM”. This offers significant improvements over SAVA and other single-point FFT approaches for analysis of in vitro ciliated cells: first, it requires no user input, thus removing the most important source of bias and reducing significantly the time required for analysis; second, as will be detailed in the following sections, it is a technique that intrinsically extracts physical quantities averaged over the sample, improving statistics over single-point techniques (it can be easily tuned to maintain the spatial information, if this is desired). However, the most notable advantage of multiscale-DDM over point-FFT approaches is that DDM measures various physical quantities of the cilia dynamics that might be related to diseases, thus providing doctors and researchers with full information for diagnostics.

*What is DDM?* DDM is a near-field (or deep-Fresnel) technique that relies on the Fourier analysis of difference images to retrieve information about dynamics in a sample (61). In some simple conditions, such as colloidal particle diffusion, this technique delivers the same information usually accessed by dynamic light scattering. This is possible because, as derived in Ferri et al. (63) and Giavazzi et al. (64), in near-field conditions the light intensity measured by the microscope gives direct access to the real part of the scattering field.

In a typical imaging experiment a microscope video is acquired via a camera. The raw input data are thus time-lapse images  $F(\vec{r}, t)$ , where  $\vec{r}$  is the position vector in the image plane. Let  $F(\vec{r}, t_0)$ , the frame recorded at time  $t_0$ , be the reference image, and  $D(\vec{r}, t_0, \tau)$  be the algebraic difference between the reference frame and the frame recorded at time interval  $\tau$  (i.e., lag time) after  $t_0$ , as follows:

$$D(\vec{r}, t_0, \tau) = F(\vec{r}, t_0) - F(\vec{r}, t_0 + \tau). \quad (1)$$

Then let  $D(\vec{q}, t_0, \tau)$  be the 2D Fourier transform of the differential image  $D(\vec{r}, t_0, \tau)$ . Assuming a stationary and ergodic sample (i.e., the dynamics do not depend on the reference time  $t_0$ ) it is possible to average over all

difference images with the same time  $\tau$ , obtaining the image structure function (ISF) as follows:

$$I(\vec{q}, \tau) = \langle |D(\vec{q}, t_0, \tau)|^2 \rangle_{t_0}. \quad (2)$$

If the sample is also isotropic, then the ISF will have a circular symmetry in  $\vec{q}$ . It is therefore possible to perform an azimuthal average: the image structure function  $I(q, \tau)$  now depends only on the magnitude of the scattering vector ( $q = \sqrt{q_x^2 + q_y^2}$ ) and on the lag time  $\tau$ . It is worth noting that the 2D scattering vector,  $\vec{q}$  is the projection of the 3D scattering vector  $\vec{Q}$ .

Information about the system dynamics is then obtained by looking at how the amplitude of the Fourier modes (related to  $q$ ) changes with  $\tau$ , which is the time separation between the two subtracted images. More specifically, the ISF is fitted with the following theoretical expression:

$$I(q, \tau) = A(q)[1 - f(q, \tau)] + B(q), \quad (3)$$

where  $B(q)$  is a background term that takes into account detection noise, and  $A(q)$  is the product between the intensity scattered by the sample and a transfer function that depends on the microscope.  $A(q)$  and  $B(q)$ , as it will be shown later, do not need to be known, and can be retrieved as parameters of the fit. The system dynamics are contained in  $f(q, \tau)$ , which has been shown (65,66) to be none other than the intermediate scattering function usually measured in scattering experiments, which is in turn the Fourier transform of the van Hove function  $G(\vec{r}, \tau)$  (67). It is worth noting that because of the very definition of  $f(q, \tau)$ , a decay of the latter to zero ( $f(q, \tau \rightarrow \infty) \rightarrow 0$ ) reflects the fact that sample configurations separated

by a progressively larger lag time  $\tau$  become more decorrelated due to motion in the imaged sample (68).

As a side note, exploiting the linearity of the Fourier transform, one can rearrange Eq. 2 as follows:

$$I(\vec{q}, \tau) = \langle |\mathcal{F}(F(\vec{r}, t_0)) - \mathcal{F}(F(\vec{r}, t_0 + \tau))|^2 \rangle_{t_0}, \quad (4)$$

where  $\mathcal{F}$  denotes the Fourier transform. This is computationally advantageous: in a video with  $N$  frames, one can compute only  $N$  Fourier transforms and store them in the memory to be reused as needed, whereas, using Eq. 2, the number of FFTs to be computed can be as high as  $N(N - 1)$ .

*DDM on videos of ciliated cells.* Fig. 1 shows all steps of DDM analysis. As outlined above, the first step is to take difference images between a reference frame  $F(\vec{r}, t_0)$  and a frame recorded a time interval  $\tau$  later.

2D power spectra of differential images are then calculated. All 2D power spectra obtained by the difference of images separated by the same value of  $\tau$  are averaged, as the system dynamics is assumed to be stationary.

The next step is the azimuthal average  $q = \sqrt{q_x^2 + q_y^2}$ , possible when the 2D power spectra show radial symmetry (i.e., the system dynamics is isotropic). This is clearly not the general case in samples with planar cell polarity and metachronal waves. Nevertheless, in vitro cultures often lack directionality. Here, the anisotropy is disregarded as a first approximation, as the primary goal of the analysis outlined in this section is just the assessment of the ciliary beat frequency. An example of radially averaged power spectra  $I(q, \tau)$  is shown in Fig. 1 e. As the image structure function  $I(q, \tau)$  is a function of the two variables spatial frequency  $q$  and lag time  $\tau$ , to indicate a cross section of  $I(q, \tau)$  at a fixed value of either variable, such variable will

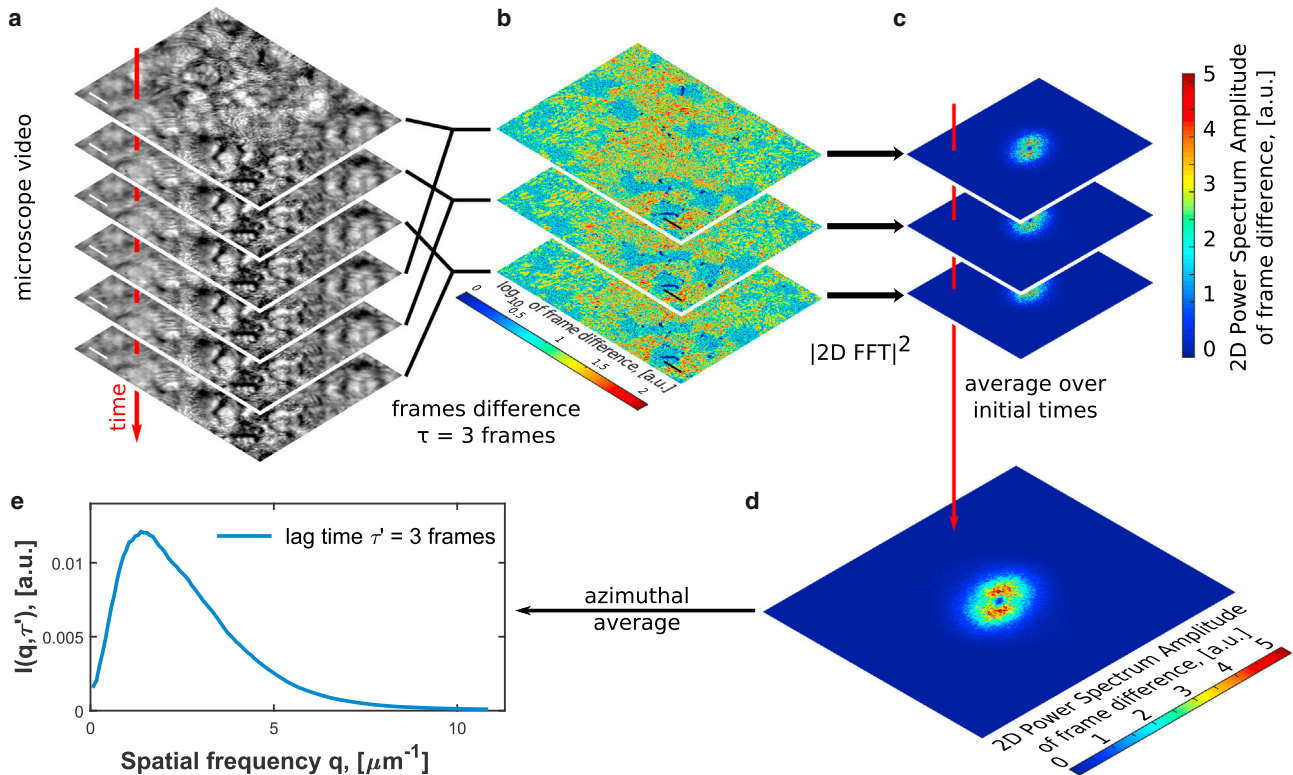


FIGURE 1 DDM allows a complete characterization of collective dynamics in ciliated cells. The technique relies on the Fourier analysis of (a) time-lapsed, bright field microscopy images. (b) Images separated by a time interval (lag time)  $\tau$  are subtracted, and (c) the absolute value of the 2D FFT of the differential images is then computed. (d) Assuming a stationary and ergodic sample we average over all the Fourier transforms of the differential images with given  $\tau$ . (e) If sample dynamics is isotropic, then the 2D power spectrum can be azimuthally averaged yielding a 1D power spectrum. To see this figure in color, go online.

be primed:  $I(q', \tau)$  is a cross section at fixed spatial frequency, whereas  $I(q, \tau')$  is a cross section at fixed lag time.

**Interpreting motile cilia DDM results.** System dynamics are accessible in the ISF by studying how the amplitude of the Fourier modes changes with  $\tau$ . The data in each  $I(q', \tau)$  (some examples shown in Fig. 2 b) behave like a damped oscillator, and can therefore be fitted with an empirical function as follows:

$$I(q', \tau) = A[1 - \exp(\cos(2\pi\nu\tau))] \exp(-\tau/\tau_c) + B. \quad (5)$$

The meaning of the fitting parameters  $A$  and  $B$  has already been discussed in What is DDM?, but for this section of particular interest are  $\nu$  and  $\tau_c$ .

The parameter  $\nu$  is the frequency of the oscillations of the amplitude of the Fourier component  $q'$ , and this is the ciliary beat frequency of the sample. As shown in Fig. 2, such frequency does not depend on the spatial frequency  $q$ . This is not (yet) a robust estimate of CBF, as in many videos the DDM signal was dominated by some high contrast impurity that would either move randomly or oscillate with a different frequency. The solution to this issue is addressed in Results and Discussion.

The other interesting parameter is the decay time  $\tau_c$ , as this is related to the coherence of cilia movement. It is sensible to expect that two factors might contribute to the decay time  $\tau_c$ . The first is a spatial factor, related to how different cilia (or cells) can beat at slightly different frequencies,

therefore not being perfectly phase-locked. This is especially due to the fact that in most of the videos in the dataset, the cilia coverage of the sample surface was patchy, with only small clumps of ciliated cells surrounded by nonciliated cells. In the hypothesis that the synchronization among cilia comes from hydrodynamic coupling (which decays as the reciprocal of the separation in the bulk, and as the reciprocal of the separation cubed close to a wall (7)), we expect to see cilia extruding from the same cell to be better synchronized than cilia belonging to different cells because of a distance effect. The second factor is that the beating cycle of one cilium might be not always identical to itself (at least because of thermal noise), and this might affect the decay time as well. A more detailed analysis of this is carried out in Appendix A using simulated data.

**DDM-based detection of metachronal waves.** Arguably the most prominent feature of a ciliated tissue is that phase-locking among beating cilia yields a metachronal wave. It is thus essential that DDM can provide insight into the metachronal wave for it to be deemed suitable for the analysis of ciliated tissues. Unfortunately, almost the entirety of in vitro samples analyzed in this article do not display long-range metachronal waves (as discussed in Interpreting Motile Cilia DDM Results, instead of a continuous carpet of cilia, the samples described in Culture of Ciliated Cells at the Air-Liquid Interface are constituted of small regions of only few ciliated cells). We believe that a possible reason for the lack of metachronal waves may be the absence (unlike the in vivo case) of flow at the moment of cilia development, and the low density of ciliated cells. Metachronal waves were therefore studied on the commercially available cultures described in Commercially Available Assay and Imaging Thereof, where despite the absence of flow during ciliary development the higher density of ciliated cells makes it possible to have some degree of long-range coordination in the ciliary beat (see Movie S1).

We found that DDM is particularly well suited to spot metachronal waves, as shown in Fig. 3 a: because a metachronal wave is a traveling wave with a well-defined wavelength  $\lambda$ , it creates a very sharp peak in the ISF at the spatial frequency corresponding to its wavenumber  $q_{\text{wave}} = 2\pi/\lambda$ . The wavelength obtained in a completely automated fashion by DDM was then cross-checked with a manual measurement, obtaining good agreement. Details of this alternative method are in Fig. 3 b and in the Supporting Material.

A second example of a DDM-based-detection metachronal wave is shown in Fig. 3, c and d: we analyzed a microscopy video published as Supporting Material in Ryser et al. (59) featuring a very well-developed metachronal wave in ovine tracheal tissue, obtaining a measurement of wavelength and propagation direction in good agreement with a manual measurement. The video was analyzed manually: as shown in Fig. 3 c, first, the slope of a line drawn along each wavefront was measured (red lines). The wavelength is then measured along a set of several parallel lines drawn perpendicularly to the wavefronts (an example is in white in Fig. 3 c). A measurement of  $\lambda$  was taken at each frame per each measurement line as the distance between two peaks of the gradient of the pixel-value cross sections along the measurement line, yielding  $\lambda = (70 \pm 2)$  px for measuring lines at  $30^\circ$  from the horizontal axis. The DDM algorithm was then run on the video, but without performing the azimuthal average on  $\vec{q}$ , to yield an image structure function  $I(\vec{q}, \tau)$ . The metachronal wave showed up in the  $I(\vec{q}, \tau)$  as a pair of sharp, symmetrical  $\vec{q}$  peaks (Fig. 3 d). The wavelength can be calculated as  $\lambda = 2\pi/|\vec{q}'|$ , whereas the propagation direction of the metachronal wave can be measured as  $\theta = \tan^{-1}(q_y/q_x)$ . As shown in Fig. 3, the manual and DDM results are in very good agreement.

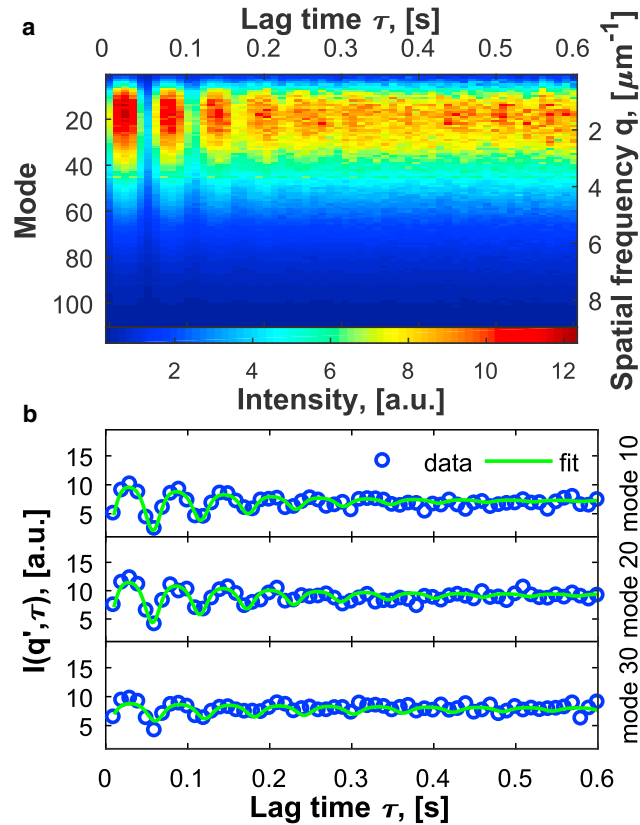
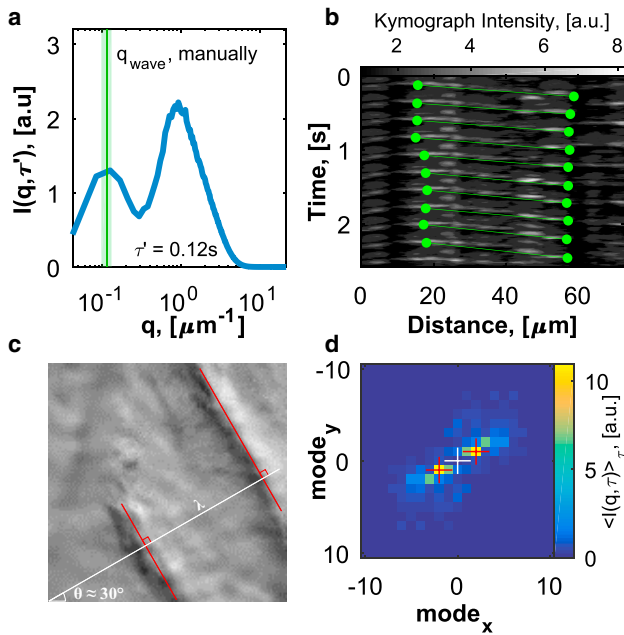


FIGURE 2 DDM measures the system dynamics. A 1D power spectrum can be computed for all possible values of the lag time  $\tau$  by repeating the steps described in Fig. 1, thus yielding (a) the image structure function  $I(q, \tau)$ . (b) The system dynamics can then be investigated through the dependence of the amplitude of each Fourier mode on the lag time  $\tau$ . In the case of a layer of ciliated cells, the Fourier mode amplitudes undergo damped oscillations, and are fitted with a suitable functions (see Eq. 5). Only three Fourier modes are shown in (b) as an example. To see this figure in color, go online.

## RESULTS AND DISCUSSION

### DDM can provide a robust estimate of CBF

In the experimental dataset described here,  $\sim 40$  videos are analyzed. Unfortunately, in several of them there is some



**FIGURE 3** DDM can detect a metachronal wave and measure its wavelength. A metachronal wave is a traveling wave with wavelength  $\lambda$ : it shows up as a sharp peak in the ISF, at  $q_{\text{wave}} = 2\pi/\lambda$ . (a) Given here is a section of the ISF at fixed lag time  $\tau'$ , showing the sharp peak at low  $q$  signature of a metachronal wave. The green line shows a direct measurement of  $q_{\text{wave}}$ , and the shaded region its standard deviation. (b) The high-speed video analyzed in (a) (Movie S1) was processed by taking the differences between subsequent frames, and calculating the local standard deviation of each differential frame (Movie S2). A kymograph was then built by taking a cross section of the processed video along a manually selected line that would follow the direction of propagation of the wave. The average slope of the characteristic regions of high intensity in this kymograph (typical of traveling waves) is the reciprocal of the wave velocity (c), and the wavenumber is then  $q_{\text{wave}} = 2\pi\nu/c$ , where  $\nu$  is the CBF. (d) Given here is the manual measurement of the metachronal wave in a microscopy video of an ovine trachea, published as Supporting Material in Ryser et al. (59). The measuring line (white) is defined to be perpendicular to the wavefronts (red lines). The wavelength is then the distance between two wavefronts along the measuring line:  $\lambda = (70 \pm 2)\text{px}$  at  $30^\circ$  from the horizontal axis. (d) The lag-time-averaged ISF of the same video clearly shows two peaks at low Fourier modes  $m_x$  and  $m_y$  (red +) symmetrical with respect to mode (0,0) (white +). Then  $\lambda = 2\pi/q = (L/\sqrt{m_x^2 + m_y^2}) = 57.3\text{px}$ , and the propagation direction is  $\theta = \tan^{-1}(q_y/q_x) = 26.6^\circ$ . The confidence intervals are  $\lambda \in [50.2, 81.0]\text{px}$ , and  $\theta \in [11.3^\circ, 45^\circ]$ , obtained assuming a  $\pm 0.5$  uncertainty on both  $m_x$  and  $m_y$ . The large confidence intervals are a direct consequence of the inherently poor spatial resolution at low Fourier modes. The manual and DDM results are in very good agreement. To see this figure in color, go online.

dirt or some other high contrast feature moving in the field of view, making the results of full-field DDM unreliable. To work around this issue, the  $720 \times 480\text{px}$  imaged region is divided into square boxes of  $80\text{-px}$  per side, which is roughly the size of a cell. The DDM algorithm is then run only on the boxes with the most activity. To select these regions, first we create a movement map of the whole movie: this is a matrix of the same size of any of the frames of the original video, and each entry contains the standard deviation

over time of the gray level of the corresponding pixels in the original video, as follows:

$$\sigma^{\text{video}}(\vec{r}) = \sqrt{\frac{1}{N-1} \sum_t (F(\vec{r}, t) - \langle F(\vec{r}, t) \rangle_t)^2},$$

where  $N$  is the number of frames and  $F(\vec{r}, t)$  is the frame recorded at time  $t$ . We then divide the field of view into boxes of the desired size, and coarse-grain the movement map by summing all the entries of it that lie within the same box. A threshold is set on the coarse-grained movement map via Otsu's method. DDM is then performed on the boxes whose movement level is over the threshold.

For each box the image structure function  $I(q, \tau)$  is obtained, and the  $\tau$ -dependence of the amplitudes of the Fourier modes is investigated by fitting  $I(q, \tau)$  curves with Eq. 5. This yields a value of the frequency  $\nu_q$  for each value of  $q$ , the average  $\langle \nu_q \rangle_q$  of which is the estimated CBF for the box. For each sample, one value of CBF for each analyzed box of each video is measured, building a distribution as shown in Fig. 4 b. The mean value of the distribution is the final (and robust) estimate of CBF in the sample, its uncertainty being the spread of the distribution. It is worth stressing that the error on CBF is not the uncertainty with which the DDM can assess a frequency, but it comes from the fact that across the sample there is a distribution of cells with different CBF, and all beating cells have been measured. Dividing the field of view into boxes proved to be an effective way to minimize the effect of debris on the measurements: when a high-contrast feature moves across a region analyzed with DDM it gives its own contribution, difficult to separate from the cilia's, to the ISF. This effect is maximum when taking DDM on the entire field of view, as the dirt will affect the only box in the video and for many frames. When dividing the field of view into many boxes instead, only the boxes on the trajectory of the debris will be affected and for fewer frames. In this way we do not need to exclude the boxes crossed by debris from the analysis, but rather we minimize the effect of this high-contrast features on the analysis. A by-product of using an (albeit rudimentary) motion-detection algorithm is the ability of providing the user with a percentage of regions showing movement. This can be useful in comparing, for example, different culture methods or stages of development. Comparisons between CBF as obtained through DDM and by using the commercial software SAVA are shown both in Fig. 4 b for a single set of 44 videos taken on the same assay in a limited amount of time, and in Fig. 4 c where the evolution of CBF in a sample is followed in time after phosphate-buffered saline was added to the sample. The results show very good agreement between DDM and SAVA measurements of CBF. It is worth stressing that CBF measurements with DDM are completely automatic, requiring no user input that might induce a bias toward faster beating (high

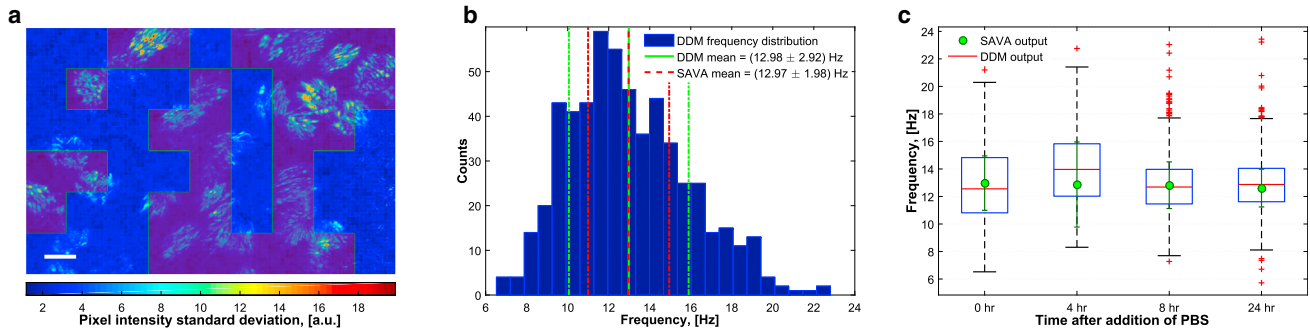


FIGURE 4 DDM can yield an accurate and robust measurement of ciliary beat frequency. Although the analysis of the entire field of view with the algorithm described in DDM on Videos of Ciliated Cells yields an accurate estimate of the average ciliary beat frequency, such measurement can be affected by stray objects (e.g., cell debris) drifting or being transported into the field of view. (a) Robustness of the analysis can be improved by dividing the field of view into small square boxes of approximately the size of a cell, and running the DDM algorithm only on the boxes with the most activity (selected by thresholding the standard deviation of pixel intensity over time), yielding one CBF value for each box. Scale bars represent  $10 \mu\text{m}$ . (b) A distribution of CBF arises when running DDM (exploiting the division of the field of view into small boxes) on 44 videos, sampling different regions of the same assay. The mean and standard deviation are shown in green, and are compared with CBF values obtained by the commercial software SAVA on the same set of videos. (c) Shown here are CBF measurements of a sample of ciliated cells, at increasing times after addition of phosphate-buffered saline. Each box shows median (central mark), 25th and 75th percentile (box), and outliers of the distribution of CBF values, extracted from  $\sim 40$  videos on the same assay. The same set of videos was analyzed with the SAVA software (green circles), showing good agreement with DDM results. To see this figure in color, go online.

frequencies). Keeping in mind that DDM can also extract other physical quantities (as described later), this is a serious improvement on the existing approaches for analyzing in vitro samples of ciliated cells.

### Multiscale-DDM can provide spatial information

Spatial information on how cilia are coupled can be recovered from the analysis of a sample with an the extension of the DDM algorithm. In the scope of this work, interesting information is whether the DDM is able to give an estimate of a length scale across which cilia beat cooperatively, if the algorithm is able to detect a metachronal wave, and how this shows up in the  $I(q, \tau)$  signal. The latter two points are discussed in DDM-based Detection of Metachronal Waves and Metachronal-wave detection. The case of in vitro cultures, where the metachronal coordination might not be evident, is where a DDM-based, multiscale approach can be powerful, particularly giving valuable information about ciliary coordination.

### Length scale of synchronization: real data

The hypothesis of a better synchronization among cilia on the same cell than across different cells is easy to verify. The resolution of all videos in the dataset described in Commercially Available Assay and Imaging Thereof is  $1920 \times 1024$  px. First, a square region of the largest possible size,  $1024 \times 1024$  px, is selected in each video and analyzed with the DDM algorithm. Then, the region is divided in smaller subregions, and the DDM is run on each one. This process of multiscale-DDM continues with the window in which the DDM runs get smaller and smaller (from  $1024 \times 1024$  px to  $16 \times 16$  px). The  $I(q, \tau)$  signal of each

window is fitted as in Eq. 5, thus extracting an amplitude, frequency, and (the one this section focuses on) decay time as a function of  $q$  for each region ( $A(q)$ ,  $\nu(q)$ ,  $\tau_c(q)$ ). Such curves are then averaged over all the regions of same size, yielding one curve  $\tau_c(q)$  for each size of the DDM window. Comparing values of  $\tau_c(q)$  as a function of the DDM window size should give insight into the length scale of synchronization. As the DDM algorithm was run on regions of different size, the range of spatial frequency  $q$  it probed is also different (although overlapping). To compare the decay time  $\tau_c(q)$  across different sizes of the analyzed region, one interval in  $q$  was selected. This interval ( $q = 2.35 \pm 0.4 \mu\text{m}^{-1}$ ) was chosen so that all  $\tau_c(q)$  curves (one for each size of the DDM window) have at least one point in it. The reciprocal of the decay time, measured at  $q \approx 2.35 \mu\text{m}^{-1}$  on all 30 videos in the dataset, is plotted in Fig. 5 b against the size of the DDM window, showing that the decay time increases dramatically when the DDM window becomes smaller than a critical area, estimated to be  $\approx 700 \mu\text{m}^2$  by fitting the data to an empirical sigmoidal curve and locating its inflection point. This value is significantly higher than the area of a single ciliated cell, whose diameter is  $\approx 10 \mu\text{m}$  (69).

## CONCLUSIONS

We have presented a new, to our knowledge, toolkit for the analysis of ciliated tissues based on differential dynamic microscopy, extending to multiscale-DDM, proving this to be a valuable tool to measure the ciliary beat frequency of in vitro human airways ciliated cells at the air-liquid interface. On the one hand, this yields results in agreement with point-FFT approaches but in a completely automated procedure without any user input, thus reducing a source

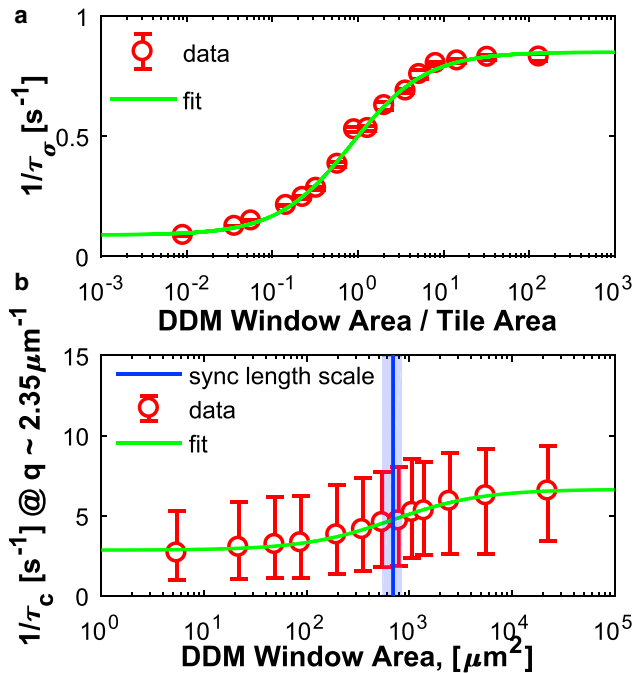


FIGURE 5 DDM can detect a characteristic length scale for synchronization. (a) The DDM algorithm was run on computer-generated data (see [Length Scale of Synchronization: Numerical Data](#)), using a grayscale matrix with pixel intensity oscillating over time, divided into phase-locked hexagonal tiles. This was done several times, changing the area (i.e., window) of DDM. Notably, the decay time  $\tau_\sigma \langle I(q, \tau) \rangle_q$  diverges when the DDM window becomes smaller than the size of a phase-locked tile. The transition is smooth because of the shape mismatch between the hexagonal tiles and the square DDM windows. The green line is an empirical fit of the data to  $1/\tau_\sigma = ax/(x + b) + c$ , where  $x$  is the DDM window area normalized over the area of the hexagonal tiles. The error on the data is comparable with the marker size. (b) In experimental data, a similar behavior is observed when plotting the reciprocal  $1/\tau_c$  of the decay time of  $I(q', \tau)$  against the size of the DDM window (following [Length Scale of Synchronization: Real Data](#)). Again the decay time diverges when the DDM algorithm is run on a small enough window; here this happens at  $\approx 700 \mu\text{m}^2$ . The red markers show the median, and the error bars the 25th and the 75th percentile for each value of the DDM window area. The green line is an empirical fit of the data to  $1/\tau_c = ax/(x + b) + c$ , whereas the blue line shows the position of its inflection point with the 95% confidence interval in shaded blue. To see this figure in color, go online.

of bias and speeding up the analysis. This suggests DDM analysis to be a serious alternative to commercial software for providing a reliable, fast, and unbiased estimate of the ciliary beat frequency, even in a clinical environment.

On the other hand, new information is retrieved using DDM compared to fixed-point FFT analysis: the algorithm gives an output signal that is closely related to the intermediate scattering function, quantifying fully the system dynamics.

Guided also by simulated data, presented in more depth in [Appendix A: Testing DDM on Synthetic Datasets](#), we have suggested new ways, to our knowledge, of extending the DDM algorithm (multiscale-DDM) to extract spatio/temporal information from the samples, namely the correlation length for cilia beating.

The analysis algorithm was also shown able to detect the presence of a large length-scale feature such as a metachronal wave, and to measure its wavelength and direction.

Being able to estimate these quantities (a length scale across which movement is coordinated, the angular spread of cilia beating, and properties of the metachronal wave) is fundamental toward a possible employment of DDM in a clinical environment, in particular to assess the structural and functional integrity of ciliated tissues. For example, we are preparing a work in which DDM is used to assess how modifying the mucus rheology affects the ciliary movement in samples from cystic fibrosis donors. This technique could also be of use in studying if and how ciliated airways tissues can recover after being damaged because of a blast wave (70), or in regenerative medicine.

The analysis scripts used during this work are available at <http://dx.doi.org/10.17863/CAM.9853>.

## APPENDIX A: TESTING DDM ON SYNTHETIC DATASETS

To conclusively demonstrate the power of DDM to extract spatio/temporal correlation, its use is explored here on datasets (synthetic videos) that have known characteristics. In particular, it is interesting to understand what can contribute to a decay of the ISF with the lag time  $\tau$ .

### Phase drift yields decay of the image structure function with the lag time

To investigate the cause of the ISF decay with the lag time, we ran the DDM algorithm on synthetic videos of oscillators. Tweaking the properties of the individual oscillators, we are able to get an insight into the decay mechanism. All the details about the synthetic dataset are in the [Supporting Material](#).

In particular, we first create a synthetic video with phase-locked oscillators that start from a random phase. This was seen to yield no decay of the ISF: as the correlation between oscillators does not decay, neither does  $I(q', \tau)$ .

The second type of synthetic video is used to investigate whether, as hypothesized in [Interpreting Motile Cilia DDM Results](#), the ISF decays because cilia within the same field of view beat with slightly different frequencies. We implement oscillators with frequencies drawn from a normal distribution centered in  $\nu_0$ , and with standard deviation  $\sigma$ , starting off at a random phase. As shown in [Fig. 6 a](#), the oscillations of the ISF in this case decay exponentially with the second power of  $\tau$ . The characteristic time of the decay, found by fitting the envelope of the  $I(q', \tau)$  curves with [Eq. S4](#), is seen to be inversely proportional to the width  $\sigma$  of the frequency distribution (see [Fig. 6, c and e](#)).

To test our second hypothesis for the decay of the ISF, which is that there is some drift in the phase of each cilium (imperfect coherence, expected at least due to thermal noise), a third type of synthetic video was devised. The oscillators here beat with the same base frequency  $\nu_0$ , but their phase undergoes a random walk with step probability  $p$ . As opposed to the previous case, the oscillations of the ISF in this case decay exponentially with  $\tau$  ([Fig. 6 b](#)). The characteristic time of the decay can be found by fitting the envelope of the  $I(q', \tau)$  curves with [Eq. S7](#), and, as shown in [Fig. 6, d and f](#), is inversely proportional to the step probability  $p$ .

Having established that at least two factors can affect the decay of the ISF, the next step is understanding how the two contributions combine.

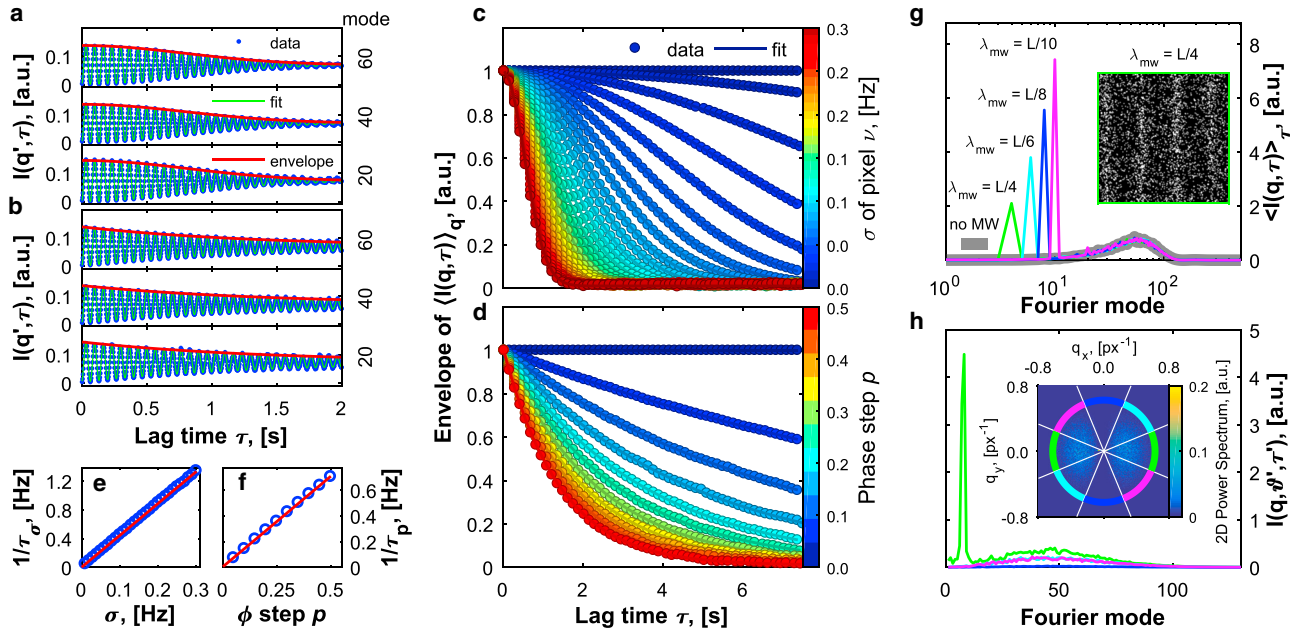


FIGURE 6 The image structure function gives access to information on phase coherence and anisotropy in the sample's dynamics. (a–f) We simulate here (see Supporting Materials and Methods) oscillators that are not completely phase-locked. The envelopes of the Fourier mode amplitudes decay with a time-scale  $\tau$ . In (a), (c), and (e), the frequencies of the oscillators are drawn from a distribution of finite width  $\sigma$ . In (b), (d), and (f) instead all the oscillators have the same frequency but their phase undergoes a random walk with step probability  $p$ . In both cases the lack of any special length scale in the simulated data yields no  $q$  dependence in the DDM output. (a and b) Behavior with  $\tau$  of the amplitude of three Fourier modes:  $I(q', \tau)$  curves are fitted (green line) with the models in Eqs. S3 and S6. Information about the decay can be obtained simply by fitting the envelopes (red lines) of the  $I(q', \tau)$  curves with Eqs. S4 and S7. (c) The same type of simulation as in (a) was repeated changing the width  $\sigma$  of the frequency distribution. Here the envelope of  $\langle I(q', \tau) \rangle_{q'}$  is drawn (dots) for various values of  $\sigma$ . The data are then fitted (continuous lines) with Eq. S4. (e) The decay time  $\tau_\sigma$  was found to be  $\propto 1/\sigma$ . (d) Similarly, the envelopes of  $\langle I(q, \tau) \rangle_{q'}$  obtained by changing the phase-step probability  $p$  are plotted (dots), and fitted (continuous lines) with Eq. S7. (f) The decay time  $\tau_p$  was found to be  $\propto 1/p$ . (g and h) DDM was run on synthetic data, generated so to have a traveling longitudinal wave moving leftwards (see Supporting Materials and Methods). (g) A traveling wave shows up as a sharp peak in the DDM signal. Changing the periodicity of the metachronal wave in the simulations (see Supporting Materials and Methods) is reflected in a change of the spatial frequency of the peak, whereas the broader maximum (due to the oscillating dots) is not affected. The inset shows a still frame from the synthetic videos. (h) Each curve is the average of the 2D power spectrum over the angles labeled with the corresponding color in the inset. The peak signature of the metachronal wave shows only in the spectrum obtained averaging the sector with  $\vartheta \in [-(\pi/8), +(\pi/8)]$ ,  $\vartheta$  being the angle between  $\vec{q}$  and the horizontal axis. The amplitude of the broader signal due to the oscillation of the dots has a maximum in this sector as well, and it goes to zero in the perpendicular direction. To see this figure in color, go online.

The DDM algorithm is thus run on a synthetic video of oscillators with frequencies drawn from a normal distribution around  $\nu_0$  with standard deviation  $\sigma$ , and whose phase undergoes a random walk with step probability  $p$ . As shown in Fig. S3 the two factors  $\sigma$  and  $p$  affect the decay independently: it is still possible to retrieve the individual decay times by fitting the envelopes of the ISF with Eq. S9, and changing either parameter only affects the corresponding decay time, but not the other.

## Metachronal-wave detection

As we saw in DDM-based Detection of Metachronal Waves, DDM is well suited to detect metachronal waves. A simple synthetic dataset was used to demonstrate, in depth, how DDM-based approach can recover metachronal-wave dynamics. The synthetic videos (details in the Supporting Material) feature finite-size oscillating dots whose initial phases are assigned to have a longitudinal wave along the  $x$  axis.

The DDM output  $I(q, \tau)$ , unsurprisingly, oscillates with  $\tau$ . More interestingly, the metachronal wave sets a spatial length scale that is highlighted by the Fourier transform. This is particularly evident when plotting the lag-time averaged 1D power spectrum (Fig. 6 g): apart from the broad maximum caused by the dots oscillating, there is also a sharp peak at smaller Fourier modes. The simulation was run changing the wavelength of the metachronal wave, and the power spectra are shown in Fig. 6 g.

The gray thick line is obtained by having the oscillating dots start from a random phase. This yields no metachronal wave, and it shows in the power spectrum  $I(q, \tau)$  as there is only one broad maximum. The green, light blue, navy, and magenta lines are the result of runs in which the metachronal wave has a wavelength of, respectively,  $1/4$ ,  $1/6$ ,  $1/8$ , and  $1/10$  the size  $L$  of the field of view. These spectra, in addition to the broad maximum, show a sharp peak each, at respective modes 4, 6, 8, and 10, which correspond to the metachronal-wave wavelengths. This shows that the peaks are the signature of the metachronal waves.

## Length scale of synchronization: numerical data

Further proof of the ability of the DDM algorithm in finding an estimate for the length scale of synchronization comes from the analysis of another specific simulation. As in Phase Drift Yields Decay of the Image Structure Function with the Lag Time and Metachronal-Wave Detection, this synthetic dataset is used to demonstrate in very controlled conditions how the multiscale-DDM approach works. The simulation is based on a gray-scale matrix of pixels with intensity oscillating in time as a sine starting off at a random phase. The matrix is divided into hexagonal tiles, and all pixels within the same tile oscillate with the same frequency. Pixels in different tiles can have different frequencies. Tile frequencies are drawn from a normal distribution peaked at  $\nu_0 = 15$  Hz and with standard

deviation  $\sigma = 0.2$  Hz. As with real data, the simulated video is divided in regions (windows) of decreasing size, and for each size all regions are analyzed with the DDM algorithm. For each region the very same analysis as in Section S3 applies, yielding a single value of the decay time  $\tau_\sigma$ . Values of  $\tau_\sigma$  measured from different windows of the same size are averaged. Fig. 5 a shows that, as in real data, the decay time  $\tau_\sigma$  diverges as the size of the DDM window becomes smaller than the size of the tile. The transition is not sharp because of the mismatch in shape between the square DDM window and the hexagonal frequency tile (i.e., each square window can probe pixels belonging to at least two different tiles). The simulation could have been carried on with square frequency tiles, but the hexagonal tiles were chosen to make the simulation closer to the real conditions, where it is highly probable that a square DDM window chosen a priori will probe cilia belonging to multiple cells.

## Anisotropic dynamics

One of the approximations made when explaining the algorithm in DDM on Videos of Ciliated Cells was to analyze the sample as if it were isotropic, thus taking a radial average of the 2D Fourier transform of differential images. This allows us to have a power spectrum that only depends on the spatial frequency, which is the magnitude of the scattering vector, discarding the direction of the latter. In a slightly more sophisticated analysis, one might want to maintain information about anisotropy in the sample when using the DDM algorithm. Let  $\vartheta$  be the angle between the scattering vector  $\vec{q}$  and the horizontal axis. An easy way of keeping the information about anisotropy is to bin  $\vartheta$  and to do a radial average only within each bin. Changing the bins allows us to tune the resolution in  $\vartheta$ , or to pick the signal only for certain ranges of  $\vartheta$  (64,71).

An example of using DDM maintaining the angular information is in Fig. 6 h, which shows a sample image from the DDM algorithm run on the simulation described in Metachronal-Wave Detection. The direction of oscillation of the dots, and, more importantly the direction of propagation of the metachronal wave, are successfully retrieved.

## SUPPORTING MATERIAL

Supporting Materials and Methods, four figures, and two movies are available at [http://www.biophysj.org/biophysj/supplemental/S0006-3495\(17\)30567-2](http://www.biophysj.org/biophysj/supplemental/S0006-3495(17)30567-2).

## AUTHOR CONTRIBUTIONS

C.J.F., L.F., and M.C. performed the experiments. M.J., L.F., and C.J.F. analyzed the data. L.F., N.B., and M.J. developed the analysis tools. P.C., C.E.B., and S.M.H. designed research. P.C. and L.F. wrote the manuscript.

## ACKNOWLEDGMENTS

We thank R. Cerbino, F. Giavazzi, M. Polin, M. Cosentino Lagomarsino, and M. Shattuck for useful discussions and comments, and J. Kotar for helping with the microscopy setup.

L.F., M.C., and P.C. are funded by the EU-ERC CoG HydroSync grant.

## REFERENCES

- Alberts, B., D. Bray, ..., A. Grimstone. 1994. *Molecular Biology of the Cell*, 3rd Ed. Garland Publishing, New York.
- Zhou, F., and S. Roy. 2015. Snapshot: motile cilia. *Cell*. 162:224–224.e1.
- Pazour, G. J., and G. B. Witman. 2003. The vertebrate primary cilium is a sensory organelle. *Curr. Opin. Cell Biol.* 15:105–110.
- Satir, P., and S. T. Christensen. 2007. Overview of structure and function of mammalian cilia. *Annu. Rev. Physiol.* 69:377–400.
- Delling, M., A. A. Indzhykulyan, ..., D. E. Clapham. 2016. Primary cilia are not calcium-responsive mechanosensors. *Nature*. 531:656–660.
- Bray, D. 2000. *Cell Movements: From Molecules to Motility*. Garland Publishing, New York.
- Bruot, N., and P. Cicuta. 2016. Realizing the physics of motile cilia synchronization with driven colloids. *Annu. Rev. Condens. Matter Phys.* 7:323–348.
- Riedel-Kruse, I. H., A. Hilfinger, ..., F. Jülicher. 2007. How molecular motors shape the flagellar beat. *HFSP J.* 1:192–208.
- Guo, H., and E. Kanso. 2016. Evaluating efficiency and robustness in cilia design. *Phys. Rev. E Stat. Nonlin. Soft Matter Phys.* 93:033119.
- Guirao, B., and J.-F. Joanny. 2007. Spontaneous creation of macroscopic flow and metachronal waves in an array of cilia. *Biophys. J.* 92:1900–1917.
- Bayly, R., and J. D. Axelrod. 2011. Pointing in the right direction: new developments in the field of planar cell polarity. *Nat. Rev. Genet.* 12:385–391.
- Stubbs, J. L., E. K. Vladar, ..., C. Kintner. 2012. Multicilin promotes centriole assembly and ciliogenesis during multiciliate cell differentiation. *Nat. Cell Biol.* 14:140–147.
- Vladar, E. K., R. D. Bayly, ..., J. D. Axelrod. 2012. Microtubules enable the planar cell polarity of airway cilia. *Curr. Biol.* 22:2203–2212.
- Smith, A. A., T. D. Johnson, ..., J. R. Blake. 2012. Symmetry breaking cilia-driven flow in the zebrafish embryo. *J. Fluid Mech.* 705:26–45.
- Biggrove, B. W., and H. J. Yost. 2006. The roles of cilia in developmental disorders and disease. *Development*. 133:4131–4143.
- Fowler, C. J. 2013. Identification of a ciliary defect associated with pulmonary nontuberculous mycobacterial disease. PhD thesis (University of Cambridge).
- Benmerah, A., B. Durand, ..., P. Bastin. 2015. The more we know, the more we have to discover: an exciting future for understanding cilia and ciliopathies. *Cilia*. 4:5.
- Horani, A., and T. W. Ferkol. 2016. Primary ciliary dyskinesia and associated sensory ciliopathies. *Expert Rev. Respir. Med.* 10:569–576.
- Shields, A. R., B. L. Fiser, ..., R. Superfine. 2010. Biomimetic cilia arrays generate simultaneous pumping and mixing regimes. *Proc. Natl. Acad. Sci. USA*. 107:15670–15675.
- Sareh, S., J. Rossiter, ..., R. Goldstein. 2013. Swimming like algae: biomimetic soft artificial cilia. *J. R. Soc. Interface*. 10:20120666.
- Hilfinger, A., A. K. Chattopadhyay, and F. Jülicher. 2009. Nonlinear dynamics of cilia and flagella. *Phys. Rev. E Stat. Nonlin. Soft Matter Phys.* 79:051918.
- Button, B., L.-H. Cai, ..., M. Rubinstein. 2012. A periciliary brush promotes the lung health by separating the mucus layer from airway epithelia. *Science*. 337:937–941.
- Bruot, N., J. Kotar, ..., P. Cicuta. 2012. Driving potential and noise level determine the synchronization state of hydrodynamically coupled oscillators. *Phys. Rev. Lett.* 109:164103.
- Kotar, J., L. Debono, ..., P. Cicuta. 2013. Optimal hydrodynamic synchronization of colloidal rotors. *Phys. Rev. Lett.* 111:228103.
- Damet, L., G. M. Cicuta, ..., P. Cicuta. 2012. Hydrodynamically synchronized states in active colloidal arrays. *Soft Matter*. 8:8672.
- Bruot, N., and P. Cicuta. 2013. Emergence of polar order and cooperativity in hydrodynamically coupled model cilia. *J. R. Soc. Interface*. 10:20130571.
- Wong, L. B., I. F. Miller, and D. B. Yeates. 1993. Nature of the mammalian ciliary metachronal wave. *J. Appl. Physiol.* 75:458–467.

28. Cosentino Lagomarsino, M., P. Jona, and B. Bassetti. 2003. Metachronal waves for deterministic switching two-state oscillators with hydrodynamic interaction. *Phys. Rev. E Stat. Nonlin. Soft Matter Phys.* 68:021908.
29. Niedermayer, T., B. Eckhardt, and P. Lenz. 2008. Synchronization, phase locking, and metachronal wave formation in ciliary chains. *Chaos.* 18:037128.
30. Elgeti, J., and G. Gompper. 2013. Emergence of metachronal waves in cilia arrays. *Proc. Natl. Acad. Sci. USA.* 110:4470–4475.
31. Osterman, N., and A. Vilfan. 2011. Finding the ciliary beating pattern with optimal efficiency. *Proc. Natl. Acad. Sci. USA.* 108:15727–15732.
32. Salathe, M. 2007. Regulation of mammalian ciliary beating. *Annu. Rev. Physiol.* 69:401–422.
33. Gueron, S., K. Levit-Gurevich, ..., J. J. Blum. 1997. Cilia internal mechanism and metachronal coordination as the result of hydrodynamical coupling. *Proc. Natl. Acad. Sci. USA.* 94:6001–6006.
34. Brumley, D. R., M. Polin, ..., R. E. Goldstein. 2015. Metachronal waves in the flagellar beating of *Volvox* and their hydrodynamic origin. *J. R. Soc. Interface.* 12:20141358.
35. Brumley, D. R., K. Y. Wan, ..., R. E. Goldstein. 2014. Flagellar synchronization through direct hydrodynamic interactions. *eLife.* 3:e02750.
36. Brumley, D. R., N. Bruot, ..., M. Polin. 2016. Long-range interactions, wobbles, and phase defects in chains of model cilia. *Phys. Rev. Fluid.* 1:081201(R).
37. Fahy, J. V., and B. F. Dickey. 2010. Airway mucus function and dysfunction. *N. Engl. J. Med.* 363:2233–2247.
38. Beule, A. G. 2010. Physiology and pathophysiology of respiratory mucosa of the nose and the paranasal sinuses. *GMS Curr. Top. Otorhinolaryngol. Head Neck Surg.* 9:Doc07.
39. Hofmann, W., and B. Asgharian. 2003. The effect of lung structure on mucociliary clearance and particle retention in human and rat lungs. *Toxicol. Sci.* 73:448–456.
40. Tilley, A. E., M. S. Walters, ..., R. G. Crystal. 2015. Cilia dysfunction in lung disease. *Annu. Rev. Physiol.* 77:379–406.
41. Sisson, J. H., J. A. Stoner, ..., T. A. Wyatt. 2003. All-digital image capture and whole-field analysis of ciliary beat frequency. *J. Microsc.* 211:103–111.
42. Dalhamn, T., and R. Rylander. 1962. Frequency of ciliary beat measured with a photo-sensitive cell. *Nature.* 196:592–593.
43. Teichtahl, H., P. L. Wright, and R. L. G. Kirsner. 1986. Measurement of in vitro ciliary beat frequency: a television-video modification of the transmitted light technique. *Med. Biol. Eng. Comput.* 24:193–196.
44. O'Callaghan, C., K. Smith, ..., K. Priftis. 1991. Ciliary beat frequency in newborn infants. *Arch. Dis. Child.* 66:443–444.
45. Chilvers, M. A., and C. O'Callaghan. 2000. Analysis of ciliary beat pattern and beat frequency using digital high speed imaging: comparison with the photomultiplier and photodiode methods. *Thorax.* 55:314–317.
46. Olm, M. A. K., J. E. Kögler, Jr., ..., J. C. Rodrigues. 2011. Primary ciliary dyskinesia: evaluation using cilia beat frequency assessment via spectral analysis of digital microscopy images. *J. Appl. Physiol.* 111:295–302.
47. Meste, O., F. Brau, and A. Guyon. 2015. Robust estimation of the motile cilia beating frequency. *Med. Biol. Eng. Comput.* 53:1025–1035.
48. Smith, C. M., J. Djakow, ..., C. O'Callaghan. 2012. ciliaFA: a research tool for automated, high-throughput measurement of ciliary beat frequency using freely available software. *Cilia.* 1:14.
49. Parrilla, E., M. Armengot, ..., D. Moratal. 2014. Primary ciliary dyskinesia assessment by means of optical flow analysis of phase-contrast microscopy images. *Comput. Med. Imaging Graph.* 38:163–170.
50. Figl, M., M. Lechner, ..., W. Birkfellner. 2012. Automatic analysis of ciliary beat frequency using optical flow. In *Medical Imaging*. D. R. Haynor and S. Ourselin, editors. International Society for Optics and Photonics (SPIE), Bellingham, WA, p. 8314.
51. Kim, W., T. H. Han, ..., R. W. Park. 2011. An automated measurement of ciliary beating frequency using a combined optical flow and peak detection. *Healthc. Inform. Res.* 17:111–119.
52. Mantovani, G., M. Pifferi, and G. Vozzi. 2010. Automated software for analysis of ciliary beat frequency and metachronal wave orientation in primary ciliary dyskinesia. *Eur. Arch. Otorhinolaryngol.* 267:897–902.
53. Quinn, S. P., M. J. Zahid, ..., S. C. Chennubhotla. 2015. Automated identification of abnormal respiratory ciliary motion in nasal biopsies. *Sci. Transl. Med.* 7 (299):299ra124.
54. Eshel, D., and Z. Priel. 1987. Characterization of metachronal wave of beating cilia on frog's palate epithelium in tissue culture. *J. Physiol.* 388:1–8.
55. Gheber, L., and Z. Priel. 1989. Synchronization between beating cilia. *Biophys. J.* 55:183–191.
56. Gheber, L., and Z. Priel. 1994. Metachronal activity of cultured mucociliary epithelium under normal and stimulated conditions. *Cell Motil. Cytoskeleton.* 28:333–345.
57. Gheber, L., A. Korngreen, and Z. Priel. 1998. Effect of viscosity on metachrony in mucus propelling cilia. *Cell Motil. Cytoskeleton.* 39:9–20.
58. Yi, W. J., K. S. Park, ..., S. W. Nam. 2002. Directional disorder of ciliary metachronal waves using two-dimensional correlation map. *IEEE Trans. Biomed. Eng.* 49:269–273.
59. Ryser, M., A. Burn, ..., J. Rička. 2007. Functional imaging of mucociliary phenomena: high-speed digital reflection contrast microscopy. *Eur. Biophys. J.* 37:35–54.
60. Schätz, G., M. Schneiter, ..., M. H. Stoffel. 2013. Ciliary beating plane and wave propagation in the bovine oviduct. *Cells Tissues Organs (Print).* 198:457–469.
61. Cerbino, R., and V. Trappe. 2008. Differential dynamic microscopy: probing wave vector dependent dynamics with a microscope. *Phys. Rev. Lett.* 100:188102.
62. Giavazzi, F., and R. Cerbino. 2014. Digital Fourier microscopy for soft matter dynamics. *J. Opt.* 16:083001.
63. Ferri, F., A. D'Angelo, ..., R. Cerbino. 2011. Kinetics of colloidal fractal aggregation by differential dynamic microscopy. *Eur. Phys. J. Spec. Top.* 199:139–148.
64. Giavazzi, F., S. Crotti, ..., R. Cerbino. 2014. Viscoelasticity of nematic liquid crystals at a glance. *Soft Matter.* 10:3938–3949.
65. Wilson, L. G., V. A. Martinez, ..., W. C. K. Poon. 2011. Differential dynamic microscopy of bacterial motility. *Phys. Rev. Lett.* 106:018101.
66. Giavazzi, F., D. Brogioli, ..., R. Cerbino. 2009. Scattering information obtained by optical microscopy: differential dynamic microscopy and beyond. *Phys. Rev. E Stat. Nonlin. Soft Matter Phys.* 80:031403.
67. Berne, B. J., and R. Pecora. 1976. *Dynamic Light Scattering*. Wiley, Hoboken, NJ.
68. Martinez, V. A., R. Besseling, ..., W. C. K. Poon. 2012. Differential dynamic microscopy: a high-throughput method for characterizing the motility of microorganisms. *Biophys. J.* 103:1637–1647.
69. Devalia, J. L., R. J. Sapsford, ..., R. J. Davies. 1990. Culture and comparison of human bronchial and nasal epithelial cells in vitro. *Respir. Med.* 84:303–312.
70. Horrocks, C. L. 2001. Blast injuries: biophysics, pathophysiology and management principles. *J. R. Army Med. Corps.* 147:28–40.
71. Reufer, M., V. A. Martinez, ..., W. C. K. Poon. 2012. Differential dynamic microscopy for anisotropic colloidal dynamics. *Langmuir.* 28:4618–4624.